

# Effect of multi-pass friction stir processing on thermal distribution and mechanical properties of AZ91

Hoda Agha Amini Fashami<sup>1</sup>, Nasrollah Bani Mostafa Arab<sup>1,\*</sup>, Mohammad Hoseinpour Gollo<sup>1</sup>, and Bahram Nami<sup>2</sup>

<sup>1</sup> Department of Mechanical Engineering, Shahid Rajaei Teacher Training University, Tehran, Iran

<sup>2</sup> Department of Materials Engineering, Shahid Rajaei Teacher Training University, Tehran, Iran

Received: 23 January 2020 / Accepted: 15 May 2020

**Abstract.** In this paper, the effect of multi-pass friction stir processing on mechanical properties of AZ91 alloy has been studied. For this purpose, the microhardness, tensile, and creep tests were conducted at several temperatures. Optical microscopy and scanning electron micrograph were used to study the microstructure of the processed samples. The experimental results indicated that at room temperature, the microhardness, tensile, and creep strength of the processed samples as compared to the unprocessed ones increased by 23%, 29%, and 38%, respectively. Also, after friction stir processing, the tensile and creep strength of the samples at 210 °C increased by 31% and 47%. In addition, a three-dimensional model was developed to simulate two-pass friction stir processing using ABAQUS/Explicit software. This model involved the Johnson-Cook models for defining material behavior during the process and identifying the fracture criterion. To control the mesh distortion during consecutive passes, the Arbitrary Lagrangian-Eulerian technique was used. Using the developed model, the peak temperature, thermal distribution, and residual stress field during multi-pass friction stir processing on AZ91 have been studied. The empirical results indicated the beneficial influence of the multi-pass friction stir processing on the microstructure and high-temperature mechanical properties of AZ91 alloy.

**Keywords:** multi-pass friction stir processing / numerical modeling / tensile / creep / AZ91 alloy

## 1 Introduction

In recent years, magnesium alloys have attracted increasing attention due to their low density and high specific strength, which provide considerable weight saving potential in automobile and transport industries [1,2]. Among the cast Mg alloys, AZ91 is the most popular alloy because of its good casting properties [3]. However, because of the unstable secondary particles with low melting point (120 °C) located on the rough grain boundaries and in the dendritic regions, the creep and tensile strength of this alloy at high temperatures reduce [4]. Hence, this alloy cannot be used for making heavier engine components that require thermal stability up to about 200 °C. For this purpose, the severe plastic deformation approaches such as friction stir processing (FSP) is used for solving this problem. It is expected that after FSP, due to the dissolution of unstable Mg<sub>17</sub>Al<sub>12</sub> eutectic phases and distribution of secondary particles on the grain boundaries, the mechanical properties improve at high temperatures. Also, after FSP, the casting defects such as cracks, cavities,

interconnection, non-adhesion between the field, and intermetallic phase particles, which cause stress concentration and failure decrease. Nevertheless, the improvement of properties after FSP is highly dependent on the process conditions. Recently, several works attempted to develop the performance of this process and to increase the mechanical properties after performing FSP.

In recent years, many researchers [5–12] have investigated the effect of single-pass FSP on the mechanical properties of different alloys. Raja et al. [13] reported that after single-pass FSP on AZ91 alloy, the coarse dendrites in the  $\alpha$ -Mg field refined slightly, the network of secondary particles dissolved, and the mechanical properties (such as tensile and impact) at room temperature improved. Lua et al. [14] reported that after FSP, the  $\beta$ -Mg<sub>17</sub>Al<sub>12</sub> networks broke into smaller particles, but the microstructure of AZ91 alloys was not finely equiaxed.

Heidarpour et al. [15] investigated the microstructure and tensile properties of AZ91 after water-submerged FSP and non-cooled FSP. Their results show that after FSP on AZ91, the rough casting structure converted into coaxial graining, and the lattice Mg<sub>17</sub>Al<sub>12</sub> eutectic phases converted into pin-like particles on the grain boundaries. The structure of water-submerged FSP samples was more

\* e-mail: [nsrl.bani.ar@gmail.com](mailto:nsrl.bani.ar@gmail.com); [n.arab@sru.ac.ir](mailto:n.arab@sru.ac.ir)

homogenous than that of the non-cooled processed samples; however, the ductility of the specimens after submerged FSP dramatically reduced. Raja et al. [16] studied the effect of the pin length on microstructure and tensile properties during single-pass FSP. Their reports show that with increasing the pin length, tensile strength improved, whereas increasing the length of the pin caused the tool to break quickly. Govindaraju et al. [17] studied the microstructure and mechanical properties of friction stir (FS) processed AZ91D<sup>1</sup> with different heat treatment conditions. The results show that subsequent heat treatment of the FS processed specimens at multiple temperatures between 150 °C and 250 °C led to the appearance of numerous particles of the  $\beta$ -phase. After heat treatment at 200 °C, the specimens had finer grains and better mechanical properties than the FS processed specimens.

Previous studies show that during single-pass FSP, thermal accumulation and asymmetric material flow applied to the samples may result in the growth of the grains adjacent to the process regions, non-homogenous structure, and imperceptible increase or reduction of mechanical properties. Apparently, it is possible to prepare finer-grained specimens with improved strength and produce the modified wide plates through multi-pass FSP. In this section, some studies on performing multi-pass FSP have been reviewed. Chai et al. [18] subjected AZ91 magnesium plates with a thickness of 6 mm to two-pass FSP. The results show that some coarse  $\beta$ -Mg<sub>17</sub>Al<sub>12</sub> phases that existed in the first pass of FSP break and dissolve into the matrix under the action of the second pass of FSP. Lu et al. [19] conducted two-pass FSP (with water-cooling) on cast AZ91 magnesium alloy plates. Their results show that the microhardness, tensile strength, and elongation of the processed specimens are 94.7 HV, 355.5 MPa, and 31.5%, respectively, which are higher than that of the base plates. Raja et al. [20] developed a layered microstructure with three different configurations by multi-pass FSP on AZ91 magnesium alloy using three different tools with probe lengths of 7, 5, and 4 mm. They were half-thickness processed, surface modified, and full-thickness processed. They concluded that the life of the fatigue-tested samples increased with increase in the fraction of the FS processed region in AZ91 alloy. Also, they measured the texture of FS processed samples by the X-ray diffraction technique.

A review of previous studies shows that the effect of consecutive passes (more than two passes) on mechanical properties and microstructure of AZ91 at high temperatures has not yet been investigated.

In addition, some researchers investigated the effective strain [21], temperature field [22,23], microstructural changes [24] and material flow [25,26] during single-pass FSP and friction stir welding (FSW) using 2D and 3D numerical modeling. Chen et al. [27] studied numerically the effect of the process parameters (including the tool geometry, axial load, the heat transfer coefficient, contact

conditions, the tool rotational and transverse speeds) on thermal history during FSP. Aljoaba and Colegrove [28,29] investigated the material flow during FSP using the computational fluid dynamics model. Cho et al. [30] investigated the temperature distribution, and material flow during FSW using a 2D model. Ulysse [31] studied thermal history and material flow using a 3D viscoelastic model. Chiumenti et al. [32] used the sliding (Lagrangian) meshes near the pin for modeling FSP, while the rest of the meshes were the Eulerian. Some researchers used the Coupled Eulerian-Lagrangian solver to investigate the effect of process parameters [33]. The results show that the pin appearance (including length and diameter), and the tool tilt are the most effective parameters on mechanical properties. Ansari et al. [34] showed that the Coupled Eulerian-Lagrangian technique is an adequate method to study this process for adjusting the optimum process parameters; however, the modeling process using this technique was time-consuming. Guerdoux and Fourment [35] used 3D Forge3 finite element (FE) software (based on Arbitrary Lagrangian-Eulerian formulation, and automatic re-meshing technique) for estimating the material flow, temperature field, and strain distribution during FSW on aluminum alloys. As seen, many researchers modeled the single-pass FSP on different alloys. In the present work, for investigating the effect of consecutive passes on thermal and stress distributions, two-pass FSP has been modeled.

As explained, in recent years, FSP has been the subject of many research studies, and several numerical models have been presented to identify the material behavior, microstructural properties, temperature history, and stress distribution. However, few studies have been conducted on multi-pass FSP as a process to modify wide surfaces [36]. In this research, the effect of twenty- five pass FSP with 50% overlapping ratio (OR) on microstructure, microhardness, tensile, and creep strength of AZ91 alloy at several temperatures has been investigated. Also, to complete the studies, a three-dimensional model has been used to investigate the thermal history and stress distribution during multi-pass FSP on AZ91. Using this model, the maximum temperature that affects the dynamic recrystallization condition and defects formation has been determined.

In the next sections, the description of materials, equipment, tests, and FE modeling of multi-pass FSP as a function of process parameters are presented.

## 2 Materials and methods

### 2.1 Experimental procedure

The workpiece material selected for this study was magnesium alloy AZ91 in the form of casting plates with dimensions of 350 × 300 × 10 mm. The chemical composition of this alloy is Al: 8.29, Zn: 0.58, Mn: 0.30, Fe: 0.0035, Cu: 0.0093, Si: 0.021 and Mg: balanced. The physical and mechanical properties of AZ91 are given in Table 1 [37,38]. The tool was prepared from H13 tool steel with a pin size of 4 mm diameter, 4 mm length, and a flat shoulder with diameter equal to 18 mm. The tool properties are shown in Table 2 [39].

<sup>1</sup> AZ91D is a high-purity alloy that has excellent corrosion resistance. It is the most commonly used magnesium die casting alloy.

**Table 1.** Material properties of AZ91 at 25 °C [36,37].

The important properties of AZ91	Value
“Young’s modulus of elasticity (GPa)”	46
“Poisson’s Ratio”	0.33
“Thermal Conductivity (Wm <sup>-1</sup> K <sup>-1</sup> )”	72
Coefficient of Thermal Expansion (°C <sup>-1</sup> )”	2.4 × 10 <sup>-5</sup>
Density (kg m <sup>-3</sup> )	1810
Specific Heat Capacity (J kg <sup>-1</sup> °C <sup>-1</sup> )	1050
Solidus temperature (°C)	470
Liquids temperature (°C)	595

**Table 2.** Material properties of H13 [39]

The important properties of AZ91	Value
“Emissivity”	0.7
Coefficient of Thermal Expansion (°C <sup>-1</sup> )	1.17 × 10 <sup>-5</sup>
“Poisson’s Ratio”	0.3

The tool was rotated clockwise and tilted 3 degrees opposite to the processing direction with 1 mm of penetration depth. In this study, FSP was performed using the universal milling machine DECKEL FP4M with different rotational and traverse speeds. The specimens were processed under different conditions and inspected for defects such as grooves, flashes, cracks, and tunnel defects. Small defects on the surface could be detected using the liquid penetrant test according to ASME-Section V (article 6). In addition, for the detection of internal defects, the radiography test was employed according to EN1435 using panoramic XXG300s equipment. Finally, rotational speed of 1200 rpm and traverse speed of 60 mm/min were selected as the optimized values for producing defect-free samples.

The overlapping ratio is used to determine the overlapping area between two consecutive passes and is defined by equation (1) [40]. In this study, the process was performed with 50% OR according to a previous work [41].

$$OR = 1 - \left[ \frac{l}{d_{pin}} \right] \quad (1)$$

where  $l$  and  $d_{pin}$  are the distance between the centers of two consecutive passes and the pin diameter respectively. After performing multi-pass FSP on AZ91 plates, the optical microscopy (OM OLYMPUS CKX53 model) and scanning electron microscopy (SEM VEGA TESCAN-XMU model) were used to study the microstructure of the processed samples. Standard tensile test specimens with 20 mm length and a width of 6 mm were cut using wire cut electro-discharge machining according to the ASTM standard E8/E8M [42]. These samples were parallel and perpendicular to the processing path. After preparing sub-size samples, the tensile tests were performed using the Zwick Roell testing device at several temperatures (25, 140, 170, and 210 °C).

**Table 3.** The Johnson-Cook constants to define the behavior of AZ91 [43]

Parameters	A	B	C	N	M
Value	108	737	0.06180	0.636	2.551

For conducting the impression creep test, the test samples with dimensions of 8 × 8 × 8 mm were prepared. The details of the impression creep test are explained by Mahmudi et al. [43]. The creep-testing device equipped with a controllable temperature furnace was used to carry out the constant-temperature and constant-load impression creep tests with a simple cylindrical indenter having 2 mm diameter.

## 2.2 Numerical modeling for investigating the thermal distribution

### 2.2.1 Numerical model details

In this paper, the assumptions are: (1) the tool and workpiece are modeled as 3D deformable materials, (2) the friction coefficient (for investigation of the frictional energy) is independent of temperature and process conditions, (3) the thermal, physical and mechanical properties of the workpiece are temperature dependent, and (4) the free surfaces of the workpiece and the instrument are surrounded by the atmosphere at the ambient temperature.

### 2.2.2 Material model

The Johnson-Cook model has been used to identify the plastic and hardening behavior of the material during the process. This model defines the relationship between stress, strain, strain rate, and temperature. Equation (2) [44] is used to explain this model and calculate the flow stress.

$$\sigma = (A + B\varepsilon^n) \left[ 1 + C \ln \left( \frac{1 + \dot{\varepsilon}}{\dot{\varepsilon}_0} \right) \right] \left( 1 - \left[ \frac{T - T_{room}}{T_{melt} - T_{room}} \right]^m \right) \quad (2)$$

$\sigma$ : The equivalent flow stress,  $\varepsilon$ : The equivalent plastic strain,  $\dot{\varepsilon}$ : The plastic strain rate,  $\dot{\varepsilon}_0$ : The reference strain rate,  $T$ : The test temperature,  $T_{room}$ : The room temperature,  $T_{melt}$ : The melting temperature,  $A$ : The initial yield stress,  $B$ : The hardening modulus,  $n$ : The work-hardening exponent,  $C$ : The strain-rate sensitivity coefficient,  $m$ : The thermal softening coefficient.

The Johnson-Cook constants for every material are determined using the results of high strain rate tests such as “(split Hopkinson’s bar or tensile test at high temperature and strain rate).” Therefore, the Johnson-Cook model is sufficient to define the material behavior during the FSP as a process with intense plastic deformation at high strain rate. The Johnson-Cook constants of AZ91 are given in Table 3 [43].

For investigating the fracture criterion, the Johnson-Cook fracture model is a sufficient relation among the strain rate, the effective stress, and the temperature at the

**Table 4.** The Johnson-Cook constants to define the damage evolution of AZ91 [44].

Parameters	D1	D2	D3	D4	D5
Value	-0.068	0.451	-0.952	0.036	0.69

fracture time. The constants of the Johnson-Cook fracture model for AZ91 are identified in Table 4 [44]. Equation (3) [45] is used for explaining the fracture strain ( $\epsilon^f$ ). In this equation,  $\sigma^*$  is the stress at fracture time,  $\dot{\epsilon}^*$  is the plastic strain rate, and T is the test temperature.

$$\epsilon^f = [D_1 + D_2 \exp(D_3 \sigma^*)][1 + D_4 \ln \dot{\epsilon}^*][1 + D_5 T]. \quad (3)$$

### 2.2.3 Interaction and heat transfer

The convective heat transfer was defined using the Film Condition type and is temperature dependent. The heat transfer between the workpiece and the backing plate is controlled by the coefficient equal to  $8500 \text{ Wm}^{-2} \text{ K}^{-1}$ . The heat transfer coefficient from the free surfaces is  $h = 12 \text{ Wm}^{-2} \text{ K}^{-1}$  at ambient temperature ( $25^\circ \text{C}$ ) [46] and the friction coefficient is 0.4 [47].

### 2.2.4 Meshing

In this work, the workpiece and tool have been meshed with the C3D8RT<sup>2</sup> elements. This element type is “the hexahedral element with 8-nodes, each having trilinear displacement and temperature degree of freedom [48]. This element produces the uniform strain (first-order reduced integration), contains hourglass control” and is sufficient to model the thermo-mechanical processes. The workpiece has been meshed with  $\sim 42,000$  elements. Also, the Arbitrary Lagrangian-Eulerian technique was used to control the mesh distortion in cases with intense deformation such as FSP. This method utilizes a wide range of approaches for analysing the processes from the purely Lagrangian analysis in which the node motion corresponds to material motion, to purely Eulerian analysis in which the nodes remain fixed in space and material flows through the elements. Also, by scaling the masses, the stable-time increment can be increased significantly. In this work, the mass scale of the target time increment is 0.0001, and many trials had been made for adjusting this suitable mass scaling.

## 3 Results and discussion

### 3.1 The microhardness test

The hardness profiles in the stirred zone-up and stirred zone-down are shown in Figure 1. The profiles show that after multi-pass FSP, generally, the hardness of processed workpieces increased to 87 VHN (Vickers hardness number), which was 23% more than that of the base

<sup>2</sup> 8-node linear brick reduced integration hourglass control.

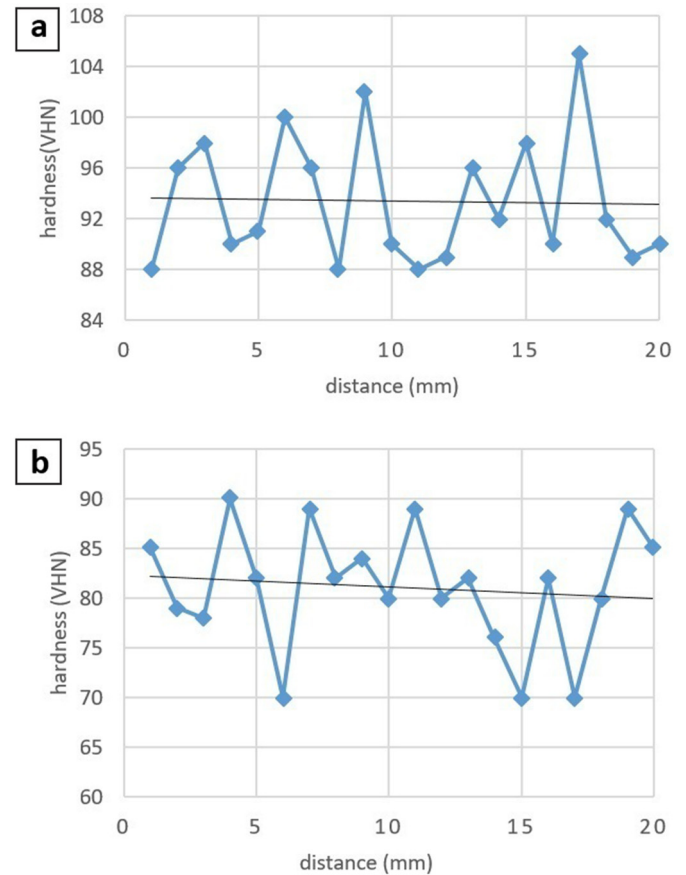


**Fig. 1.** The hardness profile in (a) the stirred zone-up, (b) the stirred zone-down.

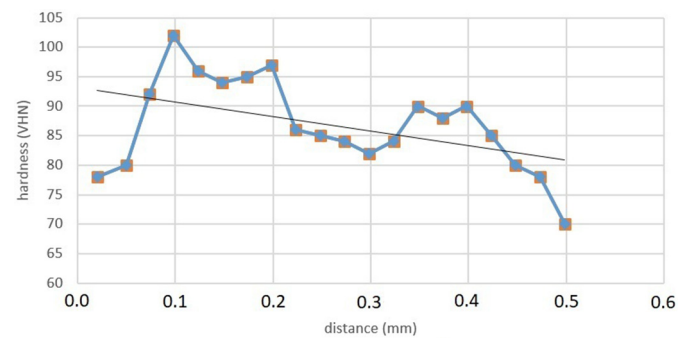


**Fig. 2.** The hardness profile along the cross section of the processed zone.

workpieces (71 VHN). Also, in Figure 2, the hardness profile along the cross-section of the processed workpiece is shown. As shown in Figures 1 and 2, the hardness of the stirred zone-up is more than the hardness of the stirred zone-down.

The microstructure of the casting plates and multi-pass processed samples were studied by OM and SEM. The samples were prepared through the standard polishing method and then etched. Figure 3 shows the microstructure of the casting samples that consists of coarse grains

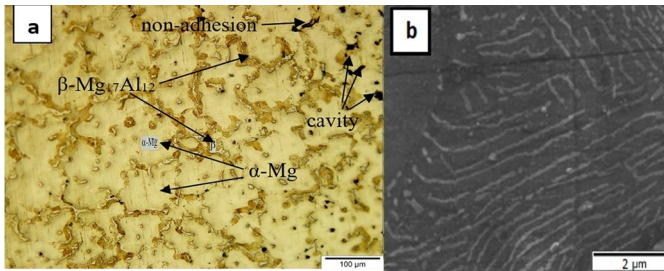


**Fig. 3.** (a) OM and (b) SEM images of the grains and casting defects of the unprocessed sample.

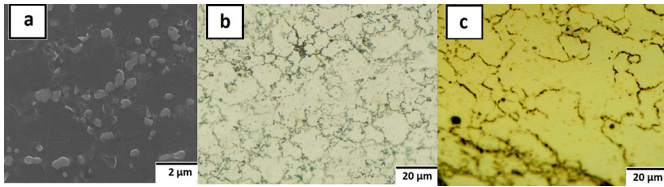


**Fig. 4.** (a) SEM image of grains and distribution of  $\beta$ -phase in field; (b) OM image of the stirred zone-down, (c) OM image of the stirred zone-up.

and the network of eutectic phases in the  $\alpha$ -Mg field. The casting defects such as cavities and non-adhesion between the field and secondary particles are observed in Figure 3a. As shown in Figure 3b,  $\alpha$ -Mg grains are surrounded by the eutectic lattice phases.

After multi-pass FSP, the microstructure refined, the grains size decreased, the eutectic lattice phases converted to spherical shape particles, and the casting defects reduced as shown in Figure 4a. Therefore, the microhardness of the processed samples increased. After multi-pass FSP, as shown in Figure 4b and c, the microstructure was non-uniform. Because of intense deformation at the tool shoulder-workpiece interface, grains in the stirred zone-up were coarser than those in the stirred zone-down, and the dislocations density in stirred zone-up is more than that in the stirred zone-down [47]. Since the microhardness of the processed samples is affected by the microstructural properties, dynamic recrystallization, texture changes, and especially the dislocations density [49]; therefore, the hardness in the stirred zone-up is more than that in the stirred zone-down.

### 3.2 The tensile test

The tensile test results for the base metal and the FS processed samples are given in Figure 5. As shown, the yield and ultimate stresses of the single-pass and multi-pass processed samples at room temperature (and parallel to the processing paths) increased by about 21% and 29% compared to the base workpiece. Improving the mechanical properties of the processed samples can be attributed to the refinement of the grains size in the processed zone and improvement of the microstructure after multi-pass FSP. In a similar research on AZ31, Feng et al. [5] reported that reducing the grain size increases strength. On the other hand, the recrystallization process reduces the density of dislocations. The competition between reducing the

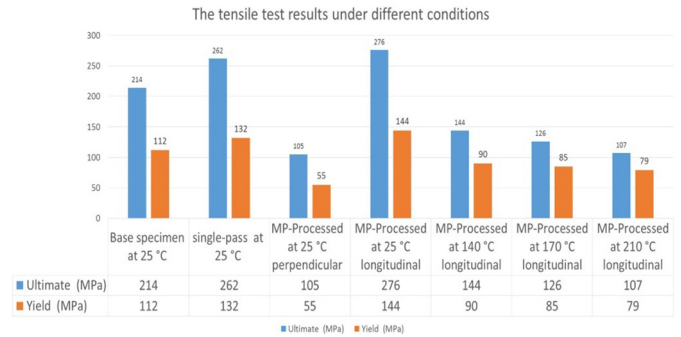


**Fig. 5.** The results of tensile tests conducted on base specimen and processed workpieces.

strength caused by decreasing the dislocations density and increasing the strength caused by reducing the grain size, affects the hardness and tensile properties. In this research, the effect of reducing grain size is more effective, and the strength increased. Besides, after performing FSP, because of the elimination of defects and crushing the unstable lattice intermetallic phases into the matrix, the microstructure and mechanical properties, especially at high temperatures improved. As shown in Figure 5, the yield and ultimate stresses of multi-pass processed samples at 140, 170, and 210 °C increased by about 23% and 31% compared to the base workpieces. Reducing the tensile strength at a perpendicular direction to the processing path can be due to the development of firm basal texture in several non-perpendicular directions. Xiaoyang et al. [45] have reported a similar experience.

### 3.3 The creep test

For metallic materials, the creep rate in the steady-state stage is defined by the power-law equation. When the impression test is performed to study the creep properties, the strain rate is calculated using the penetration depth/time slope ( $V_{imp} = dh/dt$ , where  $h$  is the penetration depth of indenter and  $t$  is time). Equivalent stress is defined utilizing the relationship between the force applied to the punch and indenter diameter ( $\sigma_{imp} = 4F/\pi\phi^2$ ). Here,  $F$  is the load applied to the punch, and  $\phi$  is the indenter diameter. Using these equations and rearranging the power-law equation, the impression creep rate can be characterized by equation (4) [50]. As seen, for calculating the stress exponent  $n$ , the curve of  $\ln(V_{imp}T/G)$  against  $\ln(\sigma_{imp}/G)$  at constant temperature ( $T$ ) is plotted. Also, the activation energy  $Q_c$  can be evaluated from the curve of  $\ln(V_{imp}T/G)$  against  $(1/T)$  at constant  $(\sigma_{imp}/G)$ . The shear modulus ( $G$ ) is temperature dependent.

$$\frac{V_{imp}T}{G} = A \left( \frac{\phi c_2}{c_1^n} \right) \left( \frac{b}{d} \right)^p \left( \frac{bD_0}{k} \right)^n \left( \frac{\sigma_{imp}}{G} \right)^n \exp \left( \frac{Q_c}{RT} \right) \quad (4)$$

$A$ : The material parameter,  $c_1$  and  $c_2$ : The constants,  $b$ : The burgers vector,  $d$ : The grain size,  $p$ : The dimensionless constant,  $D_0$ : The frequency index,  $k$ : The Boltzmann's constant,  $n$ : The stress exponent,  $Q_c$ : The creep-activation energy,  $R$ : The universal gas constant.

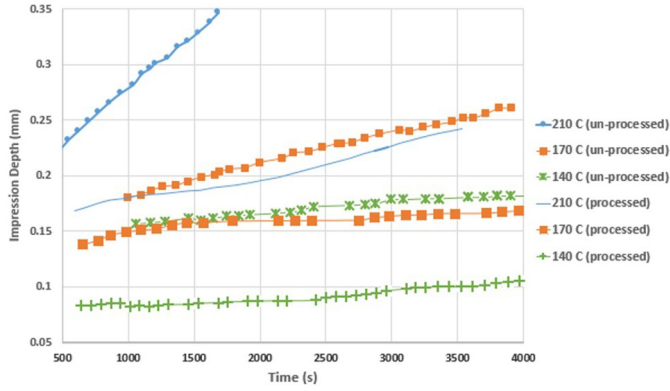


**Fig. 6.** The plot of impression depth against the time at temperatures of 140, 170, and 210 °C for the base and processed samples.

In this study, the penetration depth of the indenter after loading was measured automatically with time up to 4000s. Figure 6 shows the penetration depth of indenter at different times when the test was performed on the base samples, and FS processed samples at three temperatures of 140, 170, and 210 °C when  $\sigma_{imp}/G \sim 0.034$  is constant. Equation 5 [51] is the relation to calculate the shear modulus of AZ91 magnesium alloy at different temperatures. By calculating the impression depth/time slope in the steady-state stage and comparing the results, the effect of performing FSP and temperature on the creep rate can be investigated.

$$G = 18460 - 8.2 \times T \quad (5)$$

Where,  $G$ : The shear modulus,  $T$ : The test temperature.

As shown in Figure 6, considering the impression rate, it can be concluded that creep strength of the multi-pass processed samples at 210, 170, and 140 °C is more than that of the unprocessed samples by about 47%, 36%, and 33%, respectively. As seen in Figure 3, due to the eutectic network on the grain boundaries, the microstructure of the casting samples, especially at high temperatures was unstable. After FSP, these intermetallic  $Mg_{17}Al_{12}$  phases crushed and deformed into smaller particles. As shown in Figure 4, the size of secondary phases on the grain boundary decreased. Therefore, the harmful effects of the secondary phases on creep strength, especially at high temperatures decreased.

### 3.4 The numerical results

During FSP, the stirring operation is performed through softening, mixing, and forging actions using the rotating tool. Therefore, to prevent defects formation during the process, it is necessary to produce enough energy for sufficient stirring. In other words, the essential issue for performing FSP is the generation of enough amount of thermal energy for softening the workpiece. The plastic deformation and frictional contact should supply the necessary heat for performing this process correctly. The frictional energy depends on the friction coefficient, the

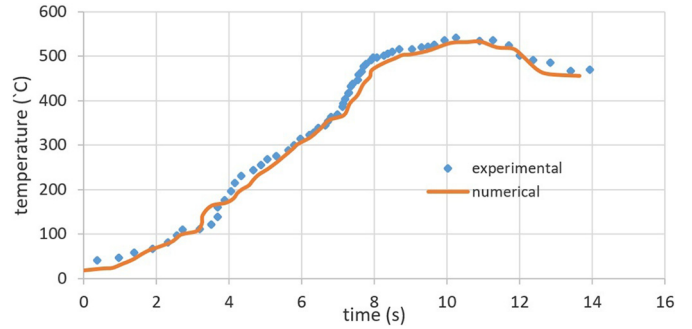


**Fig. 7.** The thermal/time profile to investigate the thermal changes at a point with 6 mm distance from the start point.

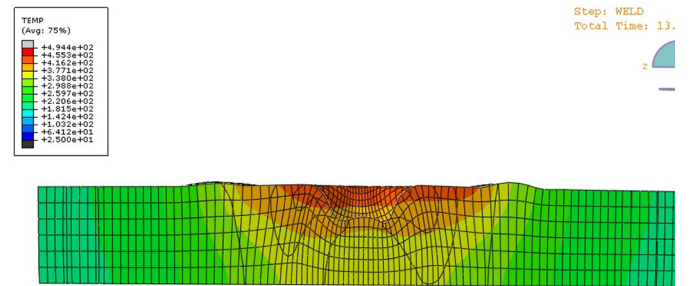


**Fig. 8.** The temperature contours along the transverse direction after 10 mm tool translation.

contact area between the tool shoulder and workpiece, the rotational speed, and the pressure applied to the tool shoulder.

For investigating the thermal aspects of this process, it is essential to determine the thermal history of some points and the temperature distribution during performing this process. In this section, the temperature distribution and thermal history obtained from numerical modeling have been compared with the empirical results of Asadi [46]. The parameters defined in this model, including dimensions, material properties, the thermal and contact conditions were the same as Asadi's work [46] and the thermal history for the point that is at a distance of 6 mm from the start point has been investigated through numerical modeling and empirical results. This comparison is shown in Figure 7 and indicates a good agreement between the experimental measurements and the modeling results. These results can be used to investigate the microstructural properties affected by temperature distribution.

Also, the temperature contour along the transverse direction after 10 mm tool translation is shown in Figure 8. As shown, the temperature distribution around the pin is asymmetric such that the maximum temperature in the advancing-side (AS) region is 494 °C. In contrast, the maximum temperature in the retreating side (RS) is about 470 °C. The reason for this observation is that as shown in Figure 9, the plastic deformation in the advancing-side region is more than plastic deformation in the retreating-side region [52]. The dissipating heat from the workpiece to the backing plate causes the contour with the "V" shape.

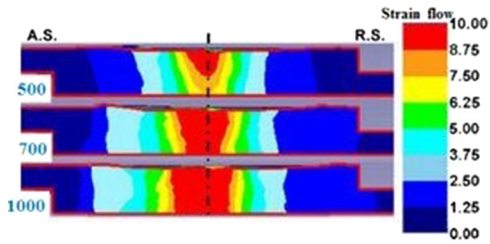


**Fig. 9.** The plastic deformation in the advancing side and retreating side regions at 500 rpm, 700 rpm and 1000 rpm [35].

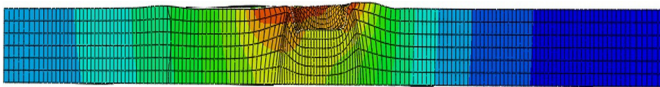


**Fig. 10.** The temperature contours along the longitudinal direction after 10 mm tool translation.

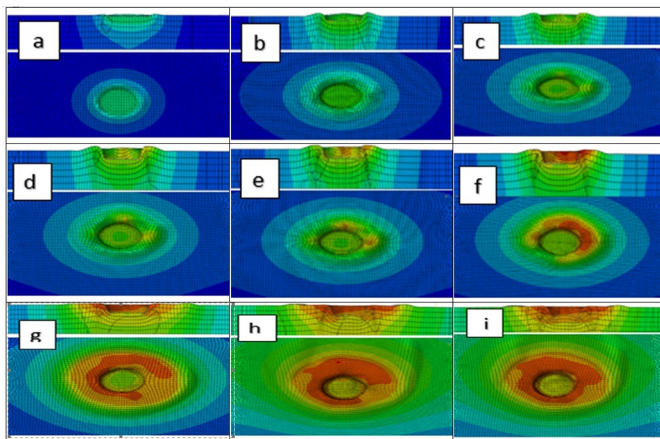


**Fig. 11.** The temperature distributions at (a) 1.5 s, (b) 4.5 s, (c) 6.3 s, (d) 6.4 s, (e) 6.6 s, (f) 7 s, (g) 8.3 s, (h) 11.6 s, and (i) 13.5 s in the first pass.

As shown in Figure 10, in the longitudinal direction, the maximum temperature is observed at the workpiece/tool-shoulder interface and behind the pin. The maximum heat generation and heat radiation dissipation occur in this region just behind the shoulder edge.

Figure 11 shows the temperature distribution at nine representative time points 1.5 s, 4.5 s, 6.3 s, 6.4 s, 6.6 s, 7 s, 8.3 s, 11.6 s, and 13.5 s in the first pass and Figure 12 shows the temperature distribution at 2 s, 5.3 s, 6.6 s, 7.3 s, 7.8 s, and 11 s in the second pass. (It is noteworthy that, during the first pass, plunge phase occurs from 0 to 8 s and traverse phase happens from 8 s to 18 s and during the second pass, plunge phase occurs from 19.64 to 28.64 s and traverse phase occurs from 28.64 to 38.64 s.) In Figures 11 and 12, in every cell, the top row picture provides the cross-section view along the progressive path, while the bottom row picture gives the view from the top. As seen, when only the pin was in contact with the surface of the sample, the maximum temperature in the workpiece occurred somewhere adjacent to the edge of the pin bottom surface. After

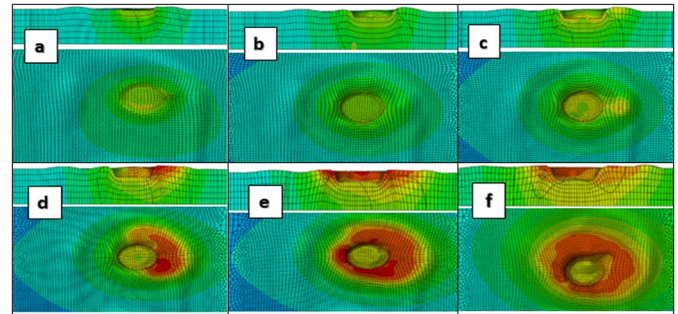


**Fig. 12.** The temperature distributions at (a) 2 s, (b) 5.3 s, (c) 6.6 s, (d) 7.3 s, (e) 7.8 s, and (f) 11 s in the second pass.

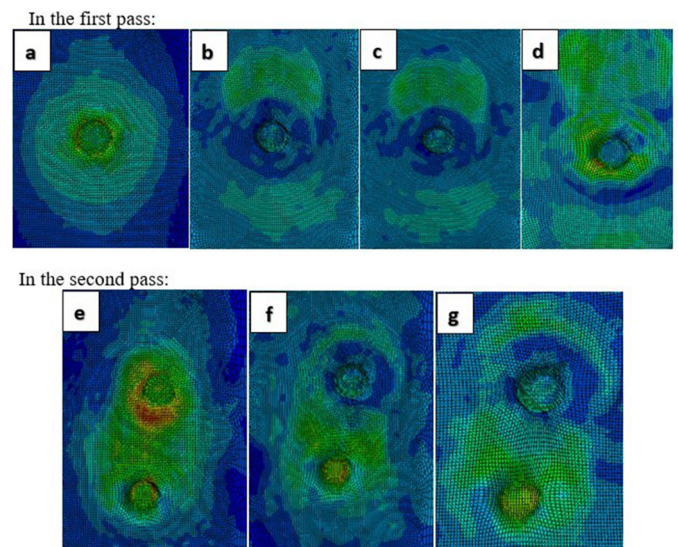


**Fig. 13.** The residual stress distribution in the longitudinal direction at (a) 3 s, (b) 13.5 s, (c) 17.7 s, and (d) 18 s in the first pass, (e) 3.1 s, (f) 7 s, and (g) 11.5 s in the second pass.

6.4 seconds, in every pass, the tool shoulder contacts the workpiece; thereafter, the region with maximum temperature moves towards the corner between the pin and shoulder surface. At 7.8 s in every pass, the full contact between tool and workpiece is established. At this time, the maximum temperature is in the tool shoulder-workpiece interface. A high-temperature gradient with “V” shape appeared in the workpiece beneath the tool, demonstrating high heat flux between the interface layer and the workpiece material outside the shoulder radius according Stephen’s work [53].

Also, Figure 13 shows the residual stress distribution in the longitudinal direction at time points 3 s, 13.5 s, 17.7 s, and 18 s in the first pass and 3.1 s, 7 s, and 11.5 s in the second pass. It is observed that the start position and end position of the process have different stress distributions as compared with the mid-position of the process. At the end position of the process, the tool during the lift up leaves the keyhole region in a compressive stress state as shown in Figure 13.

## 4 Conclusions

In this research, the effect of multi-pass FSP with 50% overlapping on tensile strength, microhardness, creep resistance, and microstructure of AZ91 magnesium alloy was investigated. In addition, a three-dimensional numerical model was simulated for this process. The Johnson-Cook model was used for defining material behavior and the failure criterion. According to the results, the following conclusions could be given:

- The microhardness of the processed samples is more than that of the base material. Also, microhardness in the stirred zone-up is more than that in the stirred zone-down.
- The yield and ultimate strength of samples after processing were more than that of the unprocessed samples by about 29%.
- Improvement of tensile and creep properties at high temperatures is far more significant than that at room temperature.
- The creep resistance of friction stir processed samples was more than that of the unprocessed ones by about 38%.
- Impression creep is a proper and fast method that gives reliable results, and an equation can be defined for characterizing the impression creep.
- The numerical results indicate that after complete contact between the tool shoulder and workpiece, the maximum temperature is found at the workpiece/shoulder interface and behind the pin.
- It was clear that the material behavior models have a significant effect on the results of the simulation. The determination of the material model constants is essential for precise simulation of the process.
- The selection of the most suitable material models, constants, heat transfer coefficient, friction coefficient, and calibrating the simulation parameters is essential for reliable modeling of the process.
- The start and end positions of the process have different stress distributions as compared with the mid position of the process. At the end position of the process, the tool during the lift up leaves the keyhole region in a compressive stress state.

## Nomenclature

$\sigma$	Equivalent stress [MPa]
$\varepsilon$	Equivalent plastic strain
$\dot{\varepsilon}$	Plastic strain rate [ $s^{-1}$ ]
$\dot{\varepsilon}_0$	Reference strain rate [ $s^{-1}$ ]
$\varepsilon^f$	Fracture strain
$A$	Initial yield stress [MPa]
$B$	Hardening modulus [MPa]
$b$	Burgers vector
$C$	Coefficient dependent on the strain rate
$d$	The tool diameter [mm]
$k$	The Boltzmann's constant
$l$	Distance between two passes [mm]
$m$	Thermal softening coefficient
$n$	The work-hardening exponent

$Q_c$	Creep-activation energy
$R$	Universal gas constant
$T_{\text{room}}$	Room temperature [K]
$T_{\text{melt}}$	Melting temperature [K]

## Authors contributions statement

Hoda Amini and Bahram Nami prepared the materials, conducted the process and experimental work. Hoda Amini modeled the process under the guidance of Mohammad Hoseinpour Gollo. All authors read and approved the manuscript. Nasrollah Bani Mostafa Arab finalized the manuscript.

The authors sincerely thank Nasrollah Bani Mostafa Arab for his critical discussion and reading during the manuscript preparation.

## References

- [1] B.L. Mordike, T. Ebert, Magnesium: Properties-applications-potential, Mater. Sci. Eng. A **302**, 37 (2001)
- [2] E. Aghion, B. Bronfin, D. Eliezer, The role of the magnesium industry in protecting the environment, J. Mater. Process. Technol. **117**, 381 (2001)
- [3] S. Fujisawa, A. Yonezu, Mechanical property of microstructure in die-cast magnesium alloy evaluated by indentation testing at elevated temperature, in: L. Ye, Recent Advances in Structural Integrity Analysis – Proceedings of the International Congress (APCF/SIF-2014), Sydney, Australia, 2014, pp. 422–426
- [4] K. Ishikawa, H. Watanabe, T. Mukai, High strain rate deformation behavior of an AZ91 magnesium alloy at elevated temperatures, Mater. Lett. **1511** (2005)
- [5] A.H. Feng, Z.Y. Ma, Enhanced mechanical properties of Mg-Al-Zn cast alloy via friction stir processing, Scr. Mater. **56**, 397 (2007)
- [6] P. Cavaliere, P.P. De Marco, Fatigue behavior of friction stir processed AZ91 magnesium alloy produced by high pressure die casting, Mater. Charact. **58**, 226 (2007)
- [7] Y. Wang, Y. Huang, X. Meng, L. Wan, J. Feng, Microstructural evolution, and mechanical properties of Mg-Zn-Y-Zr alloy during friction stir processing, J. Alloys Compd. **875** (2017)
- [8] B. Mansoor, A.K. Ghosh, Microstructure, and tensile behavior of a friction stir processed magnesium alloy, Acta Mater. **60**, 5079 (2012)
- [9] Y.S. Sato, S.H.C. Park, A. Matsunaga, A. Honda, H. Kokawa, Novel production for highly formable Mg alloy plate, J. Mater. Sci. **40**, 637 (2005)
- [10] L. Xicai, C. Genghua, Z. Wen, Q. Cheng, Z. Datong, Ductility improvement of an AZ61 magnesium alloy through two-pass submerged friction stir processing, Mater (Basel) J **10** (2017)
- [11] N. Gangil, S. Maheshwari, A.N. Siddiquee, Influence of tool pin and shoulder geometries on microstructure of friction stir processed AA6063/SiC composites, Mech. Ind. **19**, 211 (2018)
- [12] F. Kordestani, F.A. Ghasemi, N.B. Mostafa Arab, An investigation of FSW process parameters effects on mechanical properties of PP composites, Mech. Ind. **17**, 611 (2016)

- [13] A. Raja, V. Pancholi, Effect of friction stir processing on tensile, and fracture behavior of AZ91 alloy, *J. Mater. Process Tech.* **248**, 8 (2017)
- [14] Z. Lua, D. Zhangb, Microstructure, and mechanical properties of a fine-grained AZ91 magnesium, *Mater. Sci. Forum* . **850**, 778 (2016)
- [15] A. Heidarpour, S. Ahmadifard, N. Rohani, FSP pass number and cooling effect on microstructure, and properties of AZ31, *J. Adv. Mater. Process* **47** (2018)
- [16] J. Edwin, S. Shamsudeen, Optimization of multiple performance characteristics of friction stir welded joint with grey relational analysis, *J. Mater. Res.* **21**, 421 (2018)
- [17] M. Govindaraju, R.V. Vignesh, R. Padmanaban, Effect of heat treatment on the microstructure and mechanical properties of the friction stir processed AZ91D magnesium alloy, *Met. Sci. Heat Treat.* **61**, 311 (2019)
- [18] F. Chai, F. Yan, W. Wang, Q. Lu, X. Fang, Microstructures and mechanical properties of AZ91 alloys prepared by multi-pass friction stir processing, *J. Mater. Res.* **33**, 1789 (2018)
- [19] Z. Lu, D. Zhang, W. Zhang, C. Qiu, Microstructure and properties of AZ91 magnesium alloy prepared by multi-pass friction stir processing under different cooling conditions, *J. Aeronaut. Mater.* **36**, 33 (2016)
- [20] R. Allavikutty, V. Pancholi, B.K. Mishra, Layered microstructure generated by multi-pass friction stir processing in AZ91 alloy and its effect on fatigue characteristics, in: S. Seetharamu, K. Rao, R.W. Khare, *Proceedings of Fatigue, Durability and Fracture Mechanics (Lecture Notes in Mechanical Engineering)*, Springer, Singapore (2018) pp. 213–216
- [21] P. Asadi, R.A. Mahdavinjad, S. Tutunchilar, Simulation and experimental investigation of FSP of AZ91 magnesium alloy, *Mater. Sci. Eng. A* **528**, 6469 (2017)
- [22] Hibbitt, Karlsson, Sorensen (Pawtucket, R.I.), ABAQUS user manual, version 6.3, Rhode Island, 2002
- [23] Z. Yu, W. Zhang, H. Choo, Z. Feng, Transient heat and material flow modeling of friction stir processing of magnesium alloy using threaded tool, *Metall. Mater. Trans. A* **724** (2012)
- [24] H.R. Shercliff, M.J. Russell, A. Taylor, T.L. Dickerson, Microstructural modelling in friction stir welding of 2000 series aluminium alloys, *Méch. Ind.* **6**, 25 (2005)
- [25] S. Tutunchilar, M. Haghpanahi, M. Besharati Givi, Simulation of material flow in friction stir processing of a cast Al-Si alloy, *Mater. Des.* **40**, 415 (2012)
- [26] J. Rahul, K. Surjya, S. Pal, Finite element simulation of pin shape influence on material flow forces in friction stir welding, *Int. J. Adv. Manuf. Technol.* **38**, 285 (2017)
- [27] C. Chen, R. Kovacevic, Finite element modeling of friction stir welding—thermal and thermomechanical analysis, *Int. J. Mach. Tool. Manu.* **43**, 1319 (2003)
- [28] S. Aljoaba, O. Dillon, M. Khraisheh, I. Jawahir, Modeling the effects of coolant application in friction stir processing on material microstructure using 3D CFD analysis, *J. Mater. Eng. Perform.* **21**, 1141 (2013)
- [29] P.A. Colegrove, H.R. Shercliff, Dimensional CFD modelling of flow round a threaded friction stir welding tool profile, *J. Mater. Process Tech.* **169**, 320 (2005)
- [30] Y. Chao, S. Liu, C. Chien, Friction stir welding of AL 6061-T6 thick plates: Part II, numerical modeling of the thermal and heat transfer phenomena, *J. Chin. Inst. Eng.* **31**, 769 (2008)
- [31] P. Ulysse, Three-dimensional modeling of the friction-stir-welding process, *Int. J. Mach. Tools. Manuf.* **42**, 1549 (2002)
- [32] M. Chiumenti, M. Cervera, C. Agelet de Saracibar, N. Dialami, Numerical modeling of friction stir welding process, *Comput. Methods. Appl. Mech. Eng.* **254**, 353 (2013)
- [33] A. Ajri, Y. Shin, Investigation on the effects of process parameters on defect formation in friction stir welded samples via predictive numerical modeling and experiments, *J. Manuf. Sci. Eng.* **139**, 111009 (2017)
- [34] M.A. Ansari, A. Samanta, R. Abdi, H. Ding, An efficient coupled Eulerian-Lagrangian finite element model, *Int. J. Adv. Manuf. Technol.* **101**, 1495 (2019)
- [35] M. Assidi, L. Fourment, S. Guerdoux, T. Nelson, Friction model for friction stir welding process simulation: calibrations from welding experiments, *Int. J. Mach. Tools. Manuf.* **50**, 143 (2010)
- [36] S.S. Mirjavadi, M. Alipour, A.M.S. Hamouda, A. Matin, S. Kord, B.M. Afshari, P.G. Koppad, Effect of multi-pass friction stir processing on the microstructure, mechanical and wear properties of AA5083/ZrO<sub>2</sub> nanocomposites, *J. Alloy Compd.* **8**, 84 (2017)
- [37] H. Mainul, B. Latifa, Semi-continuous casting of magnesium alloy AZ91 using a filtered melt delivery system, *J. Magn. Alloy.* **3**, 283 (2015)
- [38] Y. Yuan, Q. Guo, J. Sun, High mechanical properties of AZ91 mg alloy processed by equal channel angular pressing and rolling, *Metals* **9**, 386 (2019)
- [39] G.V. Raynor, *The physical metallurgy of magnesium and its alloys*, Pergamum Press, New York, 1959
- [40] G. Venkateswarlu, D. Devaraju, M. Davidson, B. Kotiveerachari, G.R.N. Tagore, Effect of overlapping ratio on mechanical properties and formability of friction stir processed Mg AZ31B alloy, *J. Mater. Des.* **45**, 480 (2013)
- [41] A. Alizadeh, The effect of overlapping on mechanical properties of AZ91, MS theses, Maraghe University, 2016
- [42] Standard Test Methods for Tension Testing of Metallic Materials E8/E8M –13a.
- [43] R. Mahmudi, A.R. Geranmayeh, A. Rezaee, Impression creep behavior of lead-free Sn-5Sb solder alloy, *Mater. Sci. Eng.* **287** (2007)
- [44] J. Xiao, I. Ahmad, D.W. Shu, Dynamic behavior and constitutive modeling of magnesium alloys AZ91D and AZ31B under high strain rate compressive loading, *Mod. Phys. Lett. B* **28**, 1450063 (2014)
- [45] G.H. Majzooobi, F. Rahimi Dehgolan, Determination of the constants of damage models, *Proc. Eng.* **10**, 764 (2011)
- [46] V.E. Bazhenov, A.V. Petrova, A.V. Kolygin, Y.V. Tselovalnik, Determination of heat transfer coefficient between AZ91 magnesium alloy casting and no-bake mold, *Tsvetnye Metally* **89** (2017)

- [47] P. Asadi, M. besharati givi, M. Akbari, Microstructural simulation of friction stir welding using a cellular automaton method: a microstructure prediction of AZ91 magnesium alloy, *M. Int. J. Mech. Mater. Eng.* **10**, 20 (2015)
- [48] Z. Zhang, J. Bie, H. Zhang, Effect of traverse/rotational speed on material deformations and temperature distributions in friction stir welding, *J. Mater. Sci. Technol.* **24**, 907 (2008)
- [49] R.M. Miranda, J.P. Gandra, P. Vilaca, L. Quintino, T.G. Santos, *Surface modification by solid state processing*, Woodhead Publishing, United Kingdom, 2013
- [50] K.U. Kainer, *Magnesium alloys and technology*, Wiley-VCH Verlag GmbH & Co. KGaA, Weinheim, Germany, 2003
- [51] K. Ishikawa, H. Watanabe, T. Mukai, High strain rate deformation behavior of an AZ91 magnesium alloy at elevated temperatures, *Mater. Lett.* **59**, 1511 (2005)
- [52] V. Singh, S.K. Patel, A. Ranjan, B. Kuriachen, Recent research progress in solid state friction-stir welding of aluminum-magnesium alloys: a critical review, *J. Mater. Res. Technol.* (2020)
- [53] J. Stephen, V. Jayakumar, Transient Heat input Model for Friction Stir welding using non-circular Tool Pin, *FME Transactions* **48**, 137 (2020)

**Cite this article as:** H.A.A. Fashami, N.B.M. Arab, M.H. Gollo, B. Nami, Effect of multi-pass friction stir processing on thermal distribution and mechanical properties of AZ91, *Mechanics & Industry* **21**, 411 (2020)